# Multi-wavelength probes of the Milky Way's Cold Interstellar Medium: Radio Hi and Optical Ki Absorption with GASKAP and GALAH

Hiep Nguyen[1]*, Sven Buder[1,2], Juan D. Soler[3], N. M. McClure-Griffiths[1], J. R. Dawson[4,5], James Dempsey[1,6], Helga Dénes[7], John M. Dickey[8], Ian Kemp[9], Denis Leahy[10], Min-Young Lee[11], Callum Lynn[1], Yik Ki Ma[12], Antoine Marchal[1], Marc-Antoine Miville-Deschênes[13], Eric Muller[1], Claire Murray[14,15], Gyueun Park[11], Nickolas M. Pingel[16], Hilay Shah[1], Snežana Stanimirović[16], Jacco Th. van Loon[17]

[1]*Research School of Astronomy and Astrophysics, The Australian National University, Canberra, ACT 2611, Australia*
[2]*ARC Centre of Excellence for All Sky Astrophysics in 3 Dimensions (ASTRO 3D), Australia*
[3]*Istituto di Astrofisica e Planetologia Spaziali (IAPS). INAF. Via Fosso del Cavaliere 100, 00133 Roma, Italy*
[4]*Department of Physics and Astronomy and MQ Research Centre in Astronomy, Astrophysics, and Astrophotonics, Macquarie University, NSW 2109, Australia*
[5]*Australia Telescope National Facility, CSIRO Space and Astronomy, PO Box 76, Epping NSW 1710, Australia*
[6]*CSIRO Information Management and Technology, GPO Box 1700 Canberra, ACT 2601, Australia*
[7]*School of Physical Sciences and Nanotechnology, Yachay Tech University, Hacienda San José S/N, 100119, Urcuquí, Ecuador*
[8]*School of Natural Sciences, Private Bag 37, University of Tasmania, Hobart, TAS, 7001, Australia*
[9]*International Centre for Radio Astronomy Research (ICRAR), Curtin University, Bentley, WA 6102, Australia*
[10]*Department of Physics and Astronomy, University of Calgary, Calgary, AB, Canada T2N 1N4*
[11]*Korea Astronomy and Space Science Institute, 776 Daedeok-daero, Daejeon 34055, Republic of Korea*
[12]*Max-Planck-Institut für Radioastronomie, Auf dem Hügel 69, 53121 Bonn, Germany*
[13]*AIM, CEA, CNRS, Université Paris-Saclay, Université Paris Diderot, Sorbonne Paris Cité, F-91191 Gif-sur-Yvette, France*
[14]*Department of Physics & Astronomy, Johns Hopkins University, 3400 N. Charles Street, Baltimore, MD 21218, USA*
[15]*Space Telescope Science Institute, 3700 San Martin Drive, Baltimore, MD 21218, USA*
[16]*Department of Astronomy, University of Wisconsin-Madison, 475 N Charter St, Madison, WI 53703, USA*
[17]*Lennard-Jones Laboratories, Keele University, ST5 5BG, UK*

**ABSTRACT**

We present a comparative analysis of interstellar hydrogen (Hi) and potassium (Ki) absorption from the radio and optical surveys, GASKAP and GALAH, to study the physical and kinematic properties of the cold interstellar medium (ISM) in the Milky Way foreground towards the Magellanic Clouds. By comparing GASKAP Hi absorption with interstellar Ki absorption detected in GALAH spectra of nearby stars (within 12 arcmin angular distance or a spatial separation of ~0.75 pc), we reveal a strong kinematic correlation between these two tracers of the cold neutral ISM. The velocity offsets between matched Hi and Ki absorption components are small, ranging from $-6$ to $+6$ km s$^{-1}$, with a mean (median) offset of $-1.3$ ($-1.2$) km s$^{-1}$. The high degree of kinematic consistency suggests a close spatial association between Ki and cold Hi gas. Correlation analyses reveal a moderate positive relationship between Hi and Ki line-of-sight properties, such as Ki column density with Hi column density or Hi brightness temperature. We observe a ~63% overlap in the detection of both species towards 290 (out of 462) GASKAP Hi absorption lines of sight, and estimate a median Ki/Hi abundance ratio of ~$2.3 \times 10^{-10}$, in excellent agreement with previous findings. Our work opens up an exciting avenue of Galactic research that uses large-scale surveys in the radio and optical wavelengths to probe the neutral interstellar medium through its diverse tracers.

**Key words:** ISM: atoms – ISM: general – ISM: abundances – ISM: lines and bands – radio lines: ISM

## 1 INTRODUCTION

Understanding the structure, composition, and dynamics of the neutral interstellar medium (ISM) is central to unraveling the processes that govern star formation and galaxy evolution (e.g. Draine 2011; Kennicutt & Evans 2012). The neutral ISM is predominantly com-posed of atomic hydrogen (Hi) and various trace elements, including metals such as potassium (Ki), which serve as important diagnostics of its multiphase structure. Hi gas, observable via its 21-cm hyperfine transition, is the primary tracer of neutral atomic material, while neutral potassium, detected through optical absorption lines near 7699 Å, selectively probes the denser and colder regions of the atomic ISM (Trapero et al. 1995; Welty & Hobbs 2001). Together, these tracers can provide a more detailed characterisation of the physical condi-

* E-mail: vanhiep.nguyen@anu.edu.au

tions, chemical enrichment, and small-scale structure of the atomic ISM.

The neutral atomic hydrogen in the ISM exists in two main thermally stable forms: the warm neutral medium (WNM) with temperature ~8000 K and density ~0.5 cm$^{-3}$, and the cold neutral medium (CNM) with temperature ~100 K and density ~10 cm$^{-3}$, for typical Solar metallicity (Field et al. 1969; McKee & Ostriker 1977; Wolfire et al. 2003). While H I emission generally traces the bulk of the atomic gas across a wide range of temperatures and densities, H I absorption preferentially traces the CNM at lower temperatures and higher densities (Heiles & Troland 2003; Lee et al. 2015; Murray et al. 2018; Kalberla & Haud 2018; Marchal et al. 2019; Nguyen et al. 2019; McClure-Griffiths et al. 2023; Nguyen et al. 2024).

Neutral potassium K I provides an additional probe of the cold neutral medium. With a low ionization potential (4.34 eV, Corliss & Sugar 1979), K I atoms are more readily photoionized than sodium (Na I) or calcium (Ca II), resulting in a lower abundance – typically by a factor of ~15 compared to Na I and Ca II (Welty & Hobbs 2001). Consequently, significantly higher total hydrogen column densities $N_H$ are required for K I to be detectable, limiting its presence to dense, well-shielded regions where the CNM typically resides (Hobbs 1974a; Welty & Hobbs 2001). This sensitivity to high column density and shielding makes K I an effective tracer of the cold, dense components of the atomic ISM. High-resolution observations of the K I 7699 Å resonance line are particularly useful for resolving interstellar component structures in cases where the more abundant Na I lines become saturated. For instance, interstellar K I absorption has been used to investigate cool H I gas within the local ISM (Trapero et al. 1995), and to explore small-scale spatial structure in high column density environments (Lauroesch & Meyer 1999).

Recent large-scale surveys have revolutionized our ability to study ISM components in detail. In this work, we examine the Galactic ISM from the synergy between two major Galactic surveys: the Galactic Australian Square Kilometre Array Pathfinder survey (GASKAP; Dickey et al. 2013; Pingel et al. 2022) and the Galactic Archaeology with HERMES survey (GALAH; De Silva et al. 2015; Buder et al. 2025). The GASKAP-H I survey in radio provides unprecedented sensitivity and angular resolution (30 arcsec) in mapping both H I emission and absorption in the direction of the Magellanic System, including Large and Small Magellanic Clouds, Magellanic Bridge, and Magellanic Stream (e.g., McClure-Griffiths et al. 2018; Di Teodoro et al. 2019; Szotkowski et al. 2019; Dempsey et al. 2020, 2022; Ma et al. 2023; Gerrard et al. 2023; Murray et al. 2024; Chen et al. 2025; Buckland-Willis et al. 2025) as well as their Milky Way foreground (e.g., Dickey et al. 2022; Nguyen et al. 2024; Lynn et al. 2024). The GALAH optical spectroscopic survey, meanwhile, offers extensive measurements of interstellar K I absorption features toward a large sample of background stars. The combination of these data sets presents a unique opportunity to study the spatial and kinematic relations between total H I, cold H I (CNM traced by H I absorption) and the dense neutral ISM traced by interstellar K I absorption. Namely, we will investigate (*i*) the kinematic relationship between H I and K I absorption, and (*ii*) the abundance of neutral potassium relative to neutral hydrogen.

We focus on the H I gas at high Galactic latitudes in the Milky Way foreground towards the Magellanic Clouds (MCs) ($b \sim -45°$ to $-25°$). This region is characterized by distinct filamentary structures, composed of gas and dust, as illustrated in Figure 1. These filamentary structures are likely to reside close to the surface of the Local Bubble, a low-density gas-filled region formed by stellar feedback (Berkhuijsen et al. 1971; Cox & Reynolds 1987; McKee 1998; Zucker et al. 2022), at distances ~200 to 300 pc from the Sun (O'Neill

et al. 2024; Erceg et al. 2024). In this MC foreground, GASKAP-H I's large field of view (5×5 square degrees) facilitates simultaneous measurements of emission and absorption towards 2,714 background continuum sources across a 250 square degree area (Nguyen et al. 2024).

In this work, we utilize H I properties derived from GASKAP-H I absorption measurements with the Pilot II Magellanic Cloud H I foreground observations (or the GASKAP local H I survey, Nguyen et al. 2024) and K I properties obtained from GALAH Data Release 4 (Buder et al. 2025). Section 2 outlines the observational data sets from GASKAP and GALAH surveys. We then examine the kinematic relationship between interstellar K I and H I absorption in Section 3. In Section 4, we discuss H I and K I integrated properties and the K I abundances in the local ISM. Finally, Section 5 summaries our findings.

## 2 OBSERVATIONAL DATA

### 2.1 GASKAP-H I absorption and emission in radio spectra

We utilise H I absorption and emission data from the GASKAP local H I survey using on-/off-source measurements (Nguyen et al. 2024). This survey covered an area of ~250 square degrees in the direction of Magellanic Clouds, spanning a Galactic latitude range of $b = (-45°, -25°)$ and a Galactic longitude range of $l = (270°, 305°)$. The GASKAP-H I absorption pipeline developed by Dempsey et al. (2022) was employed to extract H I absorption spectra for 2,714 sources. To enhance signal-to-noise sensitivity while still resolving cold H I gas structures, the Milky Way GASKAP absorption data extending over a velocity range from $-50$ to $+50$ km s$^{-1}$, initially acquired with a native spectral resolution of 0.244 km s$^{-1}$, were smoothed to a spectral resolution of 0.977 km s$^{-1}$. Local H I absorption features were detected at the $3\sigma$ threshold towards 462 continuum background sources. Nguyen et al. (2024) then performed a Gaussian decomposition on the paired emission-absorption spectra to derive key H I physical properties: peak optical depths ($\tau_{peak}$), central velocities ($v_0$), velocity dispersions ($\Delta v_{FWHM}$) of individual absorbing gas components, spin temperatures ($T_s$) of the gas, total H I column densities ($N_{HI}$), CNM column densities ($N_{HI,CNM}$), WNM column densities ($N_{HI,WNM}$), and CNM fractions ($f_{CNM}$). Please refer to Nguyen et al. (2024) for further details.

All interstellar K I and H I emission and absorption spectra, along with their kinematic properties, H I and K I column densities, their associated uncertainties, and the data analysis notebooks used in this study, are publicly available[1].

### 2.2 GALAH DR4: Interstellar K I absorption in optical spectra

The Galactic Archaeology with HERMES (GALAH) Survey Data Release 4 (Buder et al. 2025) provides measurements of high-resolution optical stellar spectra from the High Efficiency and Resolution Multi-Element Spectrograph (HERMES) via the 2dF facility at the 3.9-m Anglo-Australian Telescope (Lewis et al. 2002; Miszalski et al. 2006; Barden et al. 2010; Brzeski et al. 2011; Heijmans et al. 2012; Farrell et al. 2014; Sheinis et al. 2015). HERMES operates with a nominal resolving power of $R = 28,000$ and covers four bands of the optical wavelength range ($471-490$, $565-587$, $648-674$, and $759-789$ nm). The spectral coverage includes several key ISM absorption features: the atomic K I absorption line at 7698.9643Å

---

[1] https://github.com/nv-hiep/gaga
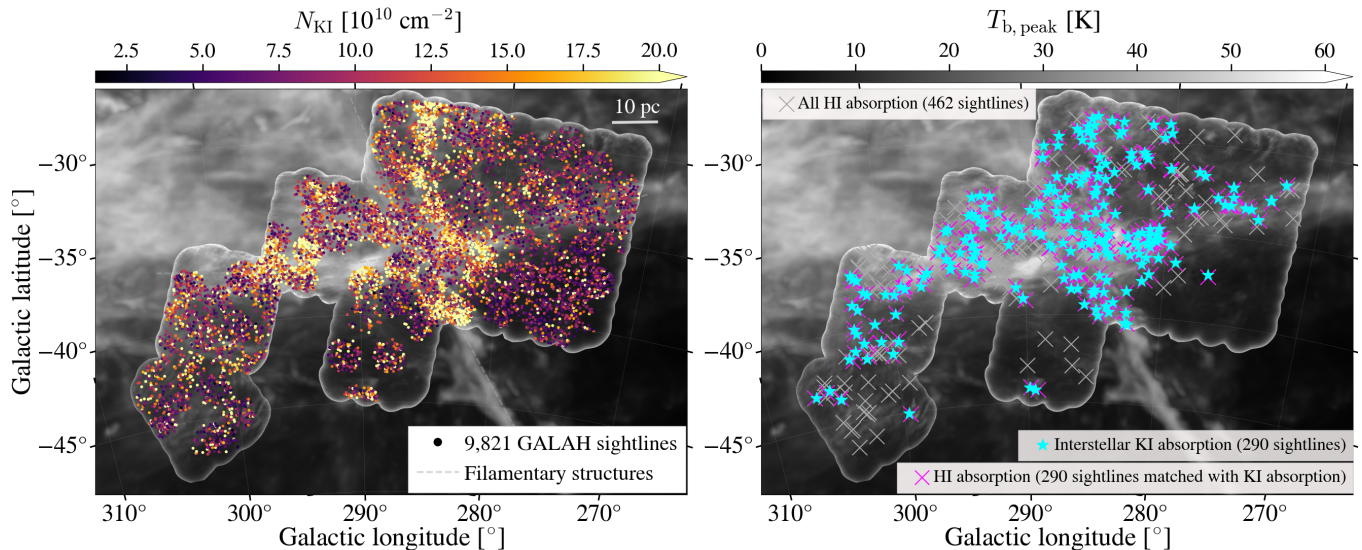
**Figure 1.** *Left panel*: Spatial on-sky distribution of GALAH K I column density measurements towards 9,821 stars in the Magellanic Cloud foreground, overlaid on the GASKAP peak brightness temperature map ($T_{b,peak}$, with an angular resolution of 30 arcsec). The gray outer boundary shows the GASKAP-H I 250-square-degree observing footprint, the GASS peak brightness is shown in the background outside this footprint. Two local H I filaments are depicted as gray dashed curves. *Right panel*: Locations of 462 background radio continuum sources ($S_{1.4\,GHz} \geq 15$ mJy) in the GASKAP-H I Pilot II survey (gray crosses) with H I detections (Nguyen et al. 2024), overlaid on the GASKAP H I peak brightness temperature map $T_{b,peak}$ (identical to the background displayed in the left panel). A subset of 290 H I absorption sightlines matched with K I absorption detections is highlighted with magenta crosses. Corresponding 290 GALAH stars with interstellar K I detections are shown as star markers. An interactive 3D view is available at github.io/gaga.

as well as diffuse interstellar band features at 5780.59Å, 5797.19Å, and 6613.66Å (Vogrinčič et al. 2023). The wavelength calibration is performed by fitting a polynomial function to the identified peak positions of ThXe emission lines from arc calibration frames (Kos et al. 2017). For the fourth band that includes the K I line, up to 31 peaks can be detected with typical root mean square values of the wavelength solution around 0.027 Å. At the K I wavelength of 7699 Å, the spectral resolution corresponds to 0.27 Å (or ~10.7 km s$^{-1}$ in velocity space). The observations are over-sampled on the CCD with a spacing of only 0.0736 Å (equivalent to 2.87 km s$^{-1}$). The wavelength calibration of optical spectra – without the use of more sophisticated methods like laser frequency combs – is typically much less precise than those of radio observations.

The analysis pipeline of GALAH DR4 fits synthetic stellar spectra, interpolated via neural networks, to the whole wavelength range in order to extract stellar parameters and elemental abundances of up to 32 elements for 917,588 stars, while iteratively shifting the observed spectrum with a global stellar radial velocity.

In modeling stellar spectra, the line spread function (accounting for instrumental and grating effects) and the rotational velocity of a star (which determines stellar rotational broadening) are taken into account. For slow rotators – particularly giant stars, which generally exhibit low rotational velocities – the intrinsic stellar K I absorption line remains narrow. As a result, it can closely resemble interstellar K I absorption. For cases where the stellar and ISM line-of-sight velocities overlap, the fitting can become degenerate and lead to over-estimated stellar K I abundances while no ISM K I can be detected in the residuals. To address this issue and disentangle stellar absorption features from interstellar counterparts, the GALAH DR4 analysis by Buder et al. (2025) implements a post-processing step in which Gaussian profiles are fitted to the residuals between observed and synthetic spectra in selected spectral regions, including those con-

taining interstellar absorption components. The fit provides not only the central wavelength to recover the line-of-sight velocity, but also the amplitude and line width (Full Width at Half Maximum, FWHM) which can be converted into an equivalent width ($EW_{KI}$). Please refer to Buder et al. (2025) for further details. We estimate the noise level in the K I absorption spectra as the standard deviation ($\sigma_{KI}$) of off-line wavelength regions.

We then select stars inside the GASKAP-H I observing footprint with (1) high K I signal-to-noise: residual flux amplitudes ($F_{KI,resid}$, the difference between the observed data and stellar model) exceeding $3\sigma_{KI}$ (three times the noise level) and K I equivalent width $EW_{KI} > 0.004$ Å; (2) ages older than 100 Myr to exclude (circum-)stellar contributions to interstellar K I content from very young stars; and (3) stellar distances $D_\star > 300$ pc, corresponding to the approximate distance to the Local Bubble shell (e.g., O'Neill et al. 2024; Leike et al. 2020, and also see Appendix A). These selection criteria result in a sample of 9,821 stars across the region of interest towards the Magellanic Cloud foreground (as shown in the left panel of Figure 1). This stellar set serves as the basis for the subsequent analysis presented in this paper.

## 3 KINEMATIC RELATIONSHIP BETWEEN INTERSTELLAR K I AND H I ABSORPTION

We examine the kinematic relationship between CNM and interstellar K I absorption features by combining data from the GASKAP-H I survey (462 H I absorption-detected lines of sight) and the GALAH DR4 catalogue (9,821 selected stars, as detailed in Section 2.2). It is worth noting that Buder et al. (2025) fitted K I absorption with a single Gaussian, while Nguyen et al. (2024) modelled the H I absorption spectra with multiple CNM Gaussian components. To establish reli-

**Table 1.** Basic information of 290 lines of sight with H I and K I detections (full table for the sources is available in the online version). For each GASKAP source, we list its Galactic longitudes/latitudes ($l$, $b$) as well as the nearby stellar Galactic longitudes/latitudes ($l^\star$, $b^\star$), the star's distance to the Sun ($D^\star$), H I and K I column densities ($N_{HI}$, $N_{KI}$), CNM central velocities ($V_{CNM}$), the corresponding matched K I absorption velocities ($V_{KI}$), and H I-K I velocity offsets ($\Delta V_{HI-KI}$).

| Source | $l$ ($^o$) | $b$ ($^o$) | $l^\star$ ($^o$) | $b^\star$ ($^o$) | $D^\star$ (pc) | $N_{HI}$ ($10^{20}$ cm$^{-2}$) | $N_{KI}$ ($10^{10}$ cm$^{-2}$) | $V_{CNM}$ (km s$^{-1}$) | $V_{KI}$ (km s$^{-1}$) | $\Delta V_{HI-KI}$ (km s$^{-1}$) |
|---|---|---|---|---|---|---|---|---|---|---|
| J002337−735529 | 305.56 | −43.06 | 305.33 | −43.02 | 1170.7 | 2.9 | 3.9 | −0.57 | 5.04 | −5.61 |
| J003414−733327 | 304.61 | −43.51 | 304.60 | −43.60 | 1482.7 | 3.0 | 6.2 | 2.88 | 3.29 | −0.41 |
| J004741−753010 | 303.25 | −41.62 | 303.45 | −41.50 | 214.5 | 3.7 | 27.3 | −0.99 | 1.52 | −2.51 |
| J005019−755629 | 303.02 | −41.19 | 302.92 | −41.14 | 1176.1 | 4.5 | 18.8 | 9.27 | 8.26 | 1.01 |
| J005321−770019 | 302.79 | −40.12 | 302.65 | −40.17 | 632.5 | 4.4 | 5.6 | 0.09 | −6.85 | 6.94 |
| J005341−771713 | 302.77 | −39.84 | 302.77 | −39.89 | 593.3 | 4.2 | 6.7 | 0.13 | 2.16 | −2.03 |
| J005641−783945 | 302.60 | −38.46 | 302.62 | −38.54 | 1689.8 | 5.2 | 16.2 | −2.12 | −1.85 | −0.27 |
| J010120−781900 | 302.29 | −38.80 | 302.30 | −38.84 | 1300.2 | 5.1 | 9.2 | −2.26 | −4.24 | 1.98 |
| J010214−801239 | 302.36 | −36.91 | 302.43 | −36.91 | 608.4 | 4.9 | 8.9 | 3.01 | 4.19 | −1.18 |
| J010249−795604 | 302.31 | −37.18 | 302.31 | −37.10 | 850.9 | 5.2 | 8.6 | 3.76 | 4.65 | −0.89 |
| J010251−753523 | 301.98 | −41.52 | 302.16 | −41.65 | 3235.1 | 4.7 | 33.0 | 9.89 | 9.39 | 0.50 |
| J010452−795246 | 302.19 | −37.23 | 302.09 | −37.21 | 759.9 | 6.0 | 8.1 | 3.64 | 4.07 | −0.43 |
| J010912−790840 | 301.87 | −37.95 | 301.70 | −37.94 | 442.0 | 5.9 | 10.9 | 2.15 | 6.98 | −4.83 |
| J011549−771147 | 301.17 | −39.85 | 301.23 | −39.80 | 1926.0 | 4.6 | 10.7 | −0.04 | −0.53 | 0.49 |
| J011552−761226 | 301.01 | −40.83 | 300.96 | −40.81 | 1723.3 | 4.2 | 8.0 | 7.33 | 8.38 | −1.05 |
| J011623−790554 | 301.44 | −37.96 | 301.51 | −38.08 | 667.8 | 5.5 | 10.2 | 3.52 | 6.10 | −2.58 |
| J012250−715042 | 299.48 | −45.07 | 299.60 | −45.04 | 1880.1 | 4.0 | 14.9 | −1.04 | 2.09 | −3.13 |
| J012257−751507 | 300.25 | −41.71 | 300.21 | −41.60 | 340.2 | 4.3 | 55.2 | −10.25 | −8.30 | −1.95 |
| J013252−760405 | 299.65 | −40.80 | 299.69 | −40.96 | 670.3 | 3.6 | 9.6 | 1.28 | 2.05 | −0.77 |
| J013910−784115 | 299.98 | −38.17 | 300.18 | −38.21 | 3520.5 | 5.8 | 6.9 | 3.54 | 3.29 | 0.25 |
| J013926−772856 | 299.59 | −39.33 | 299.63 | −39.38 | 1516.3 | 4.4 | 13.7 | 5.09 | 3.54 | 1.55 |
| J014601−783125 | 299.51 | −38.24 | 299.56 | −38.29 | 2007.4 | 6.3 | 8.1 | 2.06 | 3.61 | −1.55 |
| J015552−782819 | 298.89 | −38.15 | 298.78 | −38.02 | 608.0 | 5.6 | 10.9 | 2.80 | −0.58 | 3.38 |
| J015714−784232 | 298.90 | −37.90 | 299.02 | −37.88 | 808.0 | 6.4 | 8.9 | 2.27 | 2.21 | 0.06 |
| J020448−795503 | 298.99 | −36.64 | 299.00 | −36.66 | 2603.3 | 5.8 | 31.7 | 5.23 | 5.12 | 0.11 |
| J020803−792116 | 298.57 | −37.12 | 298.47 | −36.99 | 2033.4 | 6.0 | 12.7 | 4.00 | 4.32 | −0.32 |
| J021929−781445 | 297.38 | −37.92 | 297.60 | −37.98 | 928.6 | 6.1 | 16.3 | −1.74 | −1.90 | 0.16 |
| J022458−784143 | 297.31 | −37.39 | 297.33 | −37.45 | 465.8 | 8.0 | 23.9 | 2.53 | 4.30 | −1.77 |
| J022934−784745 | 297.12 | −37.20 | 297.06 | −37.24 | 787.3 | 7.0 | 16.4 | 2.16 | 3.14 | −0.98 |
| J024508−695753 | 289.80 | −44.15 | 289.86 | −44.18 | 879.1 | 3.8 | 16.4 | 8.58 | 12.59 | −4.01 |
| J024800−693600 | 289.21 | −44.29 | 289.43 | −44.30 | 636.1 | 3.3 | 16.2 | 9.35 | 9.88 | −0.53 |
| J025415−791927 | 296.21 | −36.15 | 296.15 | −36.19 | 1056.7 | 6.2 | 20.5 | 2.24 | 2.57 | −0.33 |
| J025618−780044 | 295.17 | −37.17 | 295.39 | −37.18 | 650.9 | 7.0 | 11.6 | 1.98 | 2.80 | −0.82 |
| J025721−782714 | 295.43 | −36.77 | 295.34 | −36.84 | 858.3 | 7.3 | 29.5 | 2.65 | 4.50 | −1.85 |
| J025803−783711 | 295.52 | −36.62 | 295.65 | −36.57 | 2661.4 | 6.5 | 16.2 | 1.97 | 3.02 | −1.05 |
| J030316−765256 | 293.94 | −37.85 | 293.73 | −37.75 | 418.7 | 5.8 | 7.8 | 1.85 | −0.42 | 2.27 |
| J030320−791455 | 295.73 | −35.96 | 295.89 | −35.89 | 698.8 | 6.7 | 16.6 | 1.93 | 2.24 | −0.31 |
| J030330−772932 | 294.39 | −37.36 | 294.33 | −37.38 | 938.5 | 7.4 | 19.9 | −0.05 | 0.92 | −0.97 |
| J031155−765150 | 293.44 | −37.55 | 293.66 | −37.54 | 1760.2 | 6.2 | 16.6 | 3.92 | 4.83 | −0.91 |
| J031235−782909 | 294.71 | −36.29 | 294.62 | −36.25 | 583.5 | 6.0 | 29.9 | 1.71 | 4.42 | −2.71 |
| J031836−795958 | 295.64 | −34.95 | 295.51 | −35.02 | 761.8 | 5.9 | 7.5 | 1.92 | 1.93 | −0.01 |
| J032019−773939 | 293.66 | −36.65 | 293.77 | −36.66 | 1021.6 | 7.0 | 25.0 | 2.57 | 4.59 | −2.02 |
| J032259−770023 | 292.97 | −37.03 | 293.08 | −36.90 | 441.7 | 7.7 | 39.4 | 5.77 | 4.68 | 1.09 |
| J032301−770029 | 292.97 | −37.03 | 293.16 | −37.01 | 1049.8 | 8.0 | 32.6 | 2.58 | 3.41 | −0.83 |
| J032456−775225 | 293.62 | −36.33 | 293.61 | −36.42 | 707.5 | 6.7 | 12.7 | 2.38 | 5.06 | −2.68 |
| J032550−735329 | 290.04 | −39.13 | 290.23 | −39.05 | 1351.3 | 5.5 | 31.1 | 8.35 | 5.59 | 2.76 |
| J032704−794916 | 295.16 | −34.83 | 295.34 | −34.91 | 216.7 | 5.9 | 9.7 | 2.37 | 6.14 | −3.77 |
| J032753−774732 | 293.41 | −36.28 | 293.48 | −36.21 | 637.6 | 8.1 | 30.3 | 2.44 | 3.83 | −1.39 |
| J032834−745053 | 290.75 | −38.33 | 290.73 | −38.43 | 445.9 | 9.9 | 21.7 | 4.78 | 7.18 | −2.40 |
| J033037−784908 | 294.17 | −35.44 | 294.19 | −35.57 | 1677.0 | 6.1 | 21.9 | 3.57 | 6.13 | −2.56 |

able matches and enable meaningful comparisons between these two datasets, we consider both spatial (on-sky) and spectral properties.

To enable direct spectral comparison, we converted the GALAH stellar spectra from wavelength to Doppler velocity in the kinematic Local Standard of Rest (LSRK) frame, using the Solar peculiar motion $(U_\odot, V_\odot, W_\odot) = (11.10, 12.24, 7.25)$ km s$^{-1}$ (Schönrich et al. 2010), where $U_\odot$ is directed towards the Galactic center, $V_\odot$ is in the direction of Galactic rotation, and $W_\odot$ points towards the north Galactic pole. This transformation ensures consistency with the velocity frame adopted in the GASKAP-H I observations. For spatial matching in the plane of sky, we adopted a search radius of 12 arcmin around each GASKAP-H I absorption sightline to identify candidate stars from the GALAH DR4 survey. Assuming a typical distance of 220 pc (see Appendix A) to the absorbing gas, this angular radius corresponds to a distance separation of ~0.75 pc. This value represents a balance between maintaining physical association with the absorbing gas and retaining a statistically significant number of matched stars.

Along the GASKAP-H I sightlines, the number of nearby GALAH stars varies between three and 14. In addition, we extended the search radius to 24 arcmin around each GASKAP-H I absorption sightline (corresponding to a linear scale of 1.5 pc) to examine how the K I-H I relation between K I and H I varies with spatial matching. In this case, the number of nearby GALAH stars per GASKAP-H I absorption detection ranges from three to 50.

Among the stars located within the 0.75 pc search radius around each GASKAP H I absorption line of sight, we select only the stars with clear separation between stellar and interstellar K I absorption features $\Delta V_{KI}^\star > 11$ km s$^{-1}$ (approximately equal to the GALAH K I spectral resolution). If multiple stars meet the criteria, the best-matched star is chosen as the one that simultaneously minimizes the velocity offset between the interstellar K I absorption feature and the nearest H I absorption Gaussian component $|\Delta V_{CNM-KI}|$ and maximizes the K I absorption amplitude. In cases where two nearby GASKAP-H I absorption sightlines are matched to the same star, we
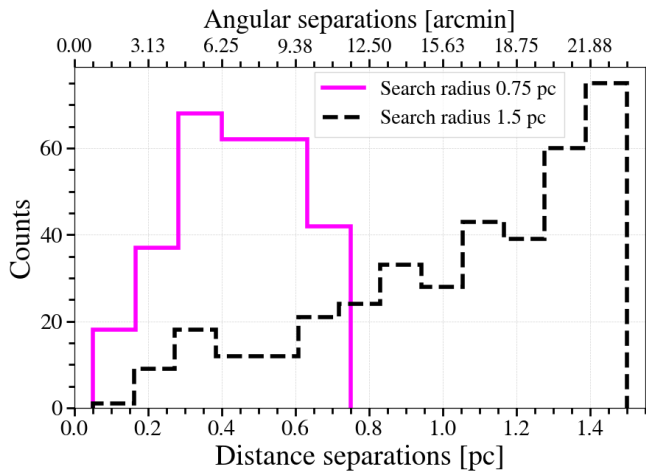
**Figure 2.** Distributions of angular and distance separations between the GASKAP-H I absorption sightlines and their corresponding matched stars. The solid line represents a sample of 290 lines of sight selected by a search radius of 0.75 pc around a GASKAP-H I absorption detection, while the dashed line represents the sample of 403 lines of sight selected within a 1.5 pc radius.

treat each sightline–star association independently, while noting that the interstellar K I absorption feature is the same in both cases. Applying this procedure, we identify 290 out of 462 GASKAP-H I lines of sight with confident detections of both H I and interstellar K I absorption, yielding a matching interstellar absorption detection rate of ~63%. When the matching radius is increased to 1.5 pc around each GASKAP-H I absorption sightline, the number of detections of both H I and interstellar K I absorption rises to 403 out of 462 sightlines, yielding a detection rate of ~87%. We will focus primarily on the 290-sightline sample with smaller search radius of 0.75 pc, while using the 403-sightline sample for comparison.

We show in Figure 1's right panel the positions of 290 matching lines of sight with both H I and interstellar K I absorption detections (magenta crosses), overlaid on the GASKAP-H I peak brightness temperature map in Galactic coordinates. An interactive 3D view is available at github.io/gaga. Table 1 summarizes their basic information, including Galactic longitudes/latitudes ($l$, $b$), corresponding stars' Galactic longitudes/latitudes ($l^\star$, $b^\star$), distance to star ($D^\star$), H I and K I column densities ($N_{HI}$, $N_{KI}$), CNM central velocities ($V_{CNM}$), the corresponding matched K I absorption velocities ($V_{KI}$), and H I-K I velocity offsets ($\Delta V_{HI-KI}$) for a sample of 50 lines of sight. A full table containing information for 290 matching H I-K I lines of sight is available in the online version of this publication.

Figure 2 shows the distributions of the angular and distance separations between the GASKAP-H I absorption sightlines and their corresponding matched stars. The solid line represents a sample of 290 sightlines with both H I and K I absorption identified within a 0.75 pc search radius around a GASKAPH I absorption detection, while the dashed line dnotes a sample of 403 sightlines obtained using a 1.5 pc radius. For the 290-sightline sample, the angular separations range from 0.45 to 11.7 arcmin. Assuming a distance of 220 pc to the local absorbing H I gas (as discussed above), these translate to physical separations of $0.03 - 0.75$ pc, with a mean, median and standard deviation of 0.44 pc, 0.44 pc and 0.17 pc, respectively.

The kinematic correlation between the central velocities of the K I and H I absorption components is shown in Figure 3 top panel, with their velocity offsets $\Delta V_{CNM-KI}$ (here $V_{0,CNM} - V_{0,KI}$) displayed in
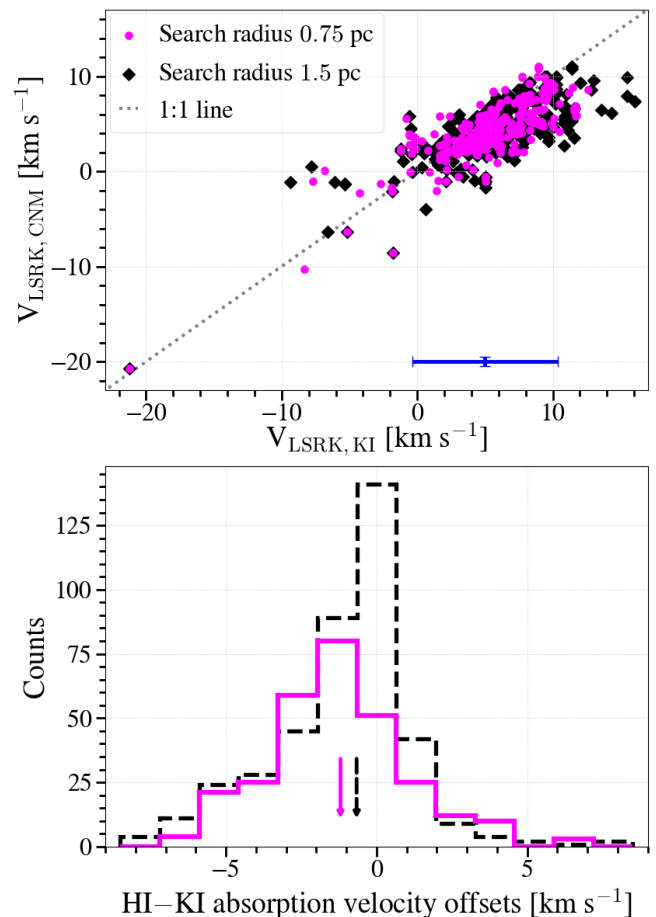


**Figure 3.** *Top panel*: Comparison of CNM and K I absorption velocities for 290 sightlines (magenta), where both H I and K I absorption were identified within a 0.75 pc search radius around a GASKAP-H I absorption detection, and for 403 sightlines (black) using a 1.5 pc radius. Error bars represent the velocity uncertainties: 0.5 km s$^{-1}$ for CNM and 5.35 km s$^{-1}$ (half the spectral resolution) for K I. *Bottom panel*: Histogram of velocity offsets between CNM and K I absorption features ($V_{CNM} - V_{KI}$): solid line for the 290-sightline sample and dashed line for the 403-sightline sample. Arrows mark their median offsets, $-1.2$ km s$^{-1}$ and $-0.7$ km s$^{-1}$, respectively.

the lower panel. The uncertainties in CNM velocities, derived from the Gaussian decomposition of GASKAP-H I spectra, are typically lower than 0.25 km s$^{-1}$ (Nguyen et al. 2024); but for simplicity, here we assume a uniform maximum uncertainty of 0.5 km s$^{-1}$ (half of the H I channel width). For the K I velocities, we adopt the GALAH K I spectral resolution of 10.7 km s$^{-1}$ as a reference, leading to an estimated uncertainty of ~5.35 km s$^{-1}$ per individual measurement (i.e., half the resolution). These velocity uncertainties are illustrated as error bars in the upper panel of Figure 3.

A strong correlation between H I and K I velocities in our sample, with Pearson (Spearman) coefficients at 0.79 (0.73) and $p-$values ~ $10^{-62}$ (~ $10^{-49}$) implies a close kinematic association between interstellar K I and CNM, indicating their co-movement and co-existence in the Galactic ISM. These results are broadly consistent with Liszt (2021), who compared higher-resolution K I spectra (R ~ 100,000 or ~3 km s$^{-1}$) obtained with the UV-Visual Echelle Spectrograph on the Very large Telescope, with H I absorption (Dickey et al. 1983) observed with the Very Large Array along five compact extragalactic continuum sources. Using a kinematic correlation coefficient defined
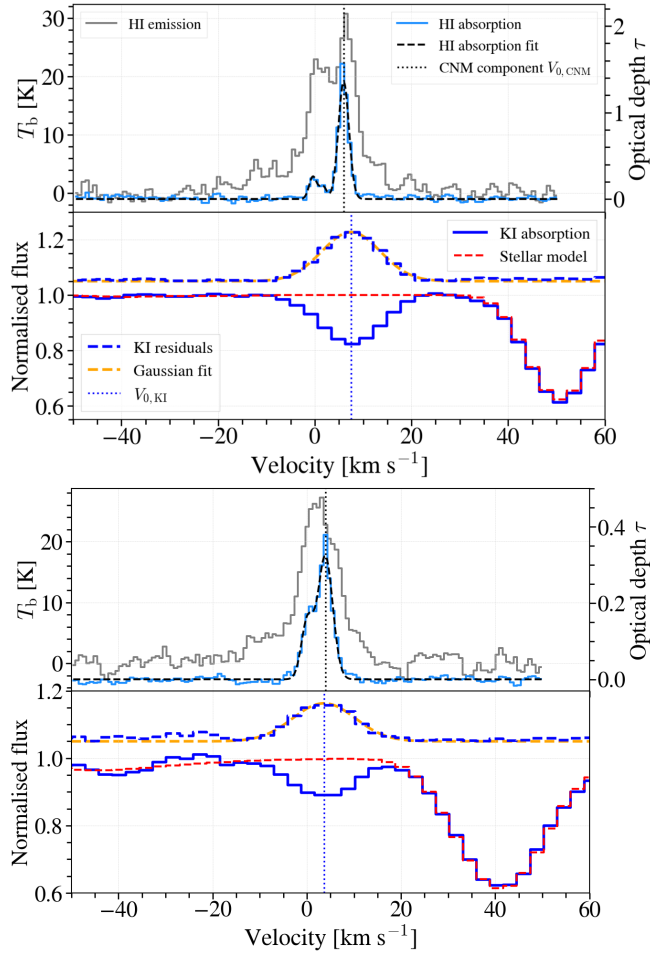
**Figure 4.** HI/KI sample spectra towards the Magellanic Cloud foreground. Top panels: HI emission (grey), absorption (light blue), and a Gaussian fit to the HI absorption profile (black dashed line). The central velocity of a CNM component is indicated by the vertical dotted line. Bottom panels: GALAH stellar spectrum (blue solid line), synthetic stellar spectrum (red solid line), residual KI absorption (blue dashed line), and a Gaussian fit to the KI residual (orange dashed line). The vertical dotted line indicates the central velocity of the KI absorption component, which aligns with the CNM central velocity. More samples are available at GASKAP Github repository.

as the velocity-space overlap integral of the absorption profiles, Liszt (2021) found values around 0.7 (see their Table 4), also indicative of a strong kinematic correspondence. Although the correlation metrics differ, both studies reveal that HI and KI absorption features are closely aligned in velocity space.

As shown in the lower panel of Figure 3, the HI-KI velocity offset distribution for the 290-sightline sample (solid line) spans from $-7$ km s$^{-1}$ to $+7$ km s$^{-1}$, with a mean of $-1.3$ km s$^{-1}$, a median of $-1.2$ km s$^{-1}$, and a standard deviation of 2.3 km s$^{-1}$. For the 403-sightline sample (dashed line), the HI–KI velocity offsets span $-8.5$ to $+8.3$, with a mean of $-1.1$ km s$^{-1}$, a median of $-0.7$ km s$^{-1}$, and a standard deviation of 2.3 km s$^{-1}$. Kolmogorov-Smirnov tests for both samples indicate that the $\Delta V_{\mathrm{CNM-KI}}$ distribution is inconsistent with a Gaussian centered at zero (KS = 0.31, $p$−value $\sim 10^{-24}$ and KS = 0.34, $p$−value $\sim 10^{-42}$, respectively), suggesting a small kinematic difference between the CNM and KI. However, given the relatively large uncertainties in the KI central velocities arising from its original spectral resolution $\sim 10.7$ km s$^{-1}$, we believe that there is no evidence
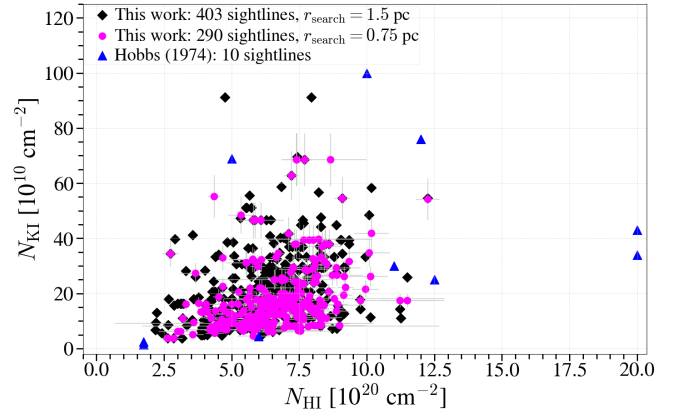
**Figure 5.** Opacity-corrected HI vs KI column densities. Circles represent our sample for 290 sightlines with a search radius of $r_{\mathrm{search}} = 0.75$ pc, diamonds show the 403-sightline sample with a 1.5 pc search radius, and triangles indicate Hobbs (1974a)'s sample of ten lines of sight.

to support real physical differences. While such differences may exist, the current KI spectral resolution does not allow us to comment on them at this level. Since the KI lines of sight are identified as close to those of HI absorption, and if we interpret velocity as a proxy for spatial location (i.e., CNM components at different velocities correspond to different distances), then our results implies that KI is likely located within or near CNM environments.

We note that whenever HI absorption is undetected along the 2,252 local GASKAP-HI sightlines (Nguyen et al. 2024), KI absorption features also tend to be absent above the $3\sigma$ threshold. Additionally, after degrading the HI spectral resolution to match that of the KI spectra, we find that interstellar KI absorption features are consistently narrower than the HI emission lines, but generally comparable in width to the HI absorption features. A higher-resolution spectroscopic study by Liszt (2021), using KI absorption spectra with $\sim 3$ km s$^{-1}$ resolution towards five HI absorption sightlines, found that KI absorption features are slightly narrower than the corresponding HI absorption features (see their Figure 1). In that work, the author analysed the line profiles of five species (HI, HCO$^+$, KI, Na I, and Ca II) along the same lines of sight, and concluded that HCO$^+$ exhibits the narrowest lines, followed in order by KI, HI, Na I, and Ca II.

## 4 INTEGRATED PROPERTIES: KI VS HI

In this Section we explore quantitative relationships between KI and HI column densities as well as the KI/HI abundance. We define the relative abundance of neutral potassium KI with respect to neutral hydrogen HI as the ratio of their respective integrated column densities, $N_{\mathrm{KI}}/N_{\mathrm{HI}}$. HI column density is obtained from the GASKAP absorption survey, and therefore is corrected for opacity effects (see Nguyen et al. 2024). The KI column density is derived from the KI equivalent width (listed in GALAH DR4 as `ew_k_is`), which is measured by Gaussian fits to the residuals between the GALAH observed spectra and the corresponding stellar models (as depicted by the blue dashed lines in Figure 4). Subsequently, assuming the interstellar KI line to be optically thin, we can employ the linear regime of the curve of growth, which establishes a direct proportionality between the KI column density $N_{\mathrm{KI}}$ and its equivalent width $EW_{\mathrm{KI}}$:

$$N_{\mathrm{KI}} \frac{\pi e^2 f \lambda^2}{m_e c^2} = \int (-\ln r_\nu) d\nu \approx EW_{\mathrm{KI}}, \tag{1}$$

with Kı wavelength $\lambda$ at 7698.9643Å, residual intensity $r_\nu$ for a frequency $\nu$, as well as electron charge $e$, electron mass $m_e$, speed of light $c$, and oscillator strength $f$ (Hobbs 1974b). For the Kı the resonance transition between the first excited electronic state to the ground electronic state ($3p^6 4p\ ^2P_{3/2} \rightarrow 3p^6 4s\ ^2S_{1/2}$), we adopted a logarithm of the oscillator strength $\log gf = -0.178$ from Trubko et al. (2017). Given the statistical weight of the lower level ($g = 2J + 1 = 2$ for the $3p^6 4s\ ^2S_{1/2}$ state with a total angular momentum $J = 1/2$) and the provided $\log gf$ value, this corresponds to an oscillator strength of $f = 0.332$.

We note that while Buder et al. (2025) provided values for the Kı equivalent width ($EW_{KI}$), Kı flux amplitude ($A_{KI}$), and the standard deviation ($\sigma_{KI}$) from Gaussian fits to the Kı absorption features, they did not report the corresponding uncertainties for these quantities. To estimate the uncertainties of the equivalent widths and the resulting column densities, we assume that the relative uncertainties for both Kı flux amplitude and the standard deviation are 10%. We then propagate these assumed uncertainties to estimate the uncertainty of the equivalent width, $\delta EW_{KI}$, using the standard error propagation formula. This results in an estimated uncertainty of ~14% for the equivalent widths. We then use this uncertainty to estimate the uncertainty in the derived Kı column densities.

Below, we perform correlation analyses using both the Hobbs (1974a) dataset (a small sample of ten lines of sight with relatively broad Galactic longitude coverage) and our own dataset consisting of 290 matched lines of sight towards the Magellanic Cloud foreground. This comparison allows us to assess the consistency and statistical significance of any potential trends between Kı and Hı column densities. In addition, we extend our analysis to a larger sample of 9,821 selected stars within the GASKAP-Hı field of view by comparing GALAH Kı column densities with GASKAP Hı peak brightness temperatures and column densities under the optically-thin assumption.

## 4.1 Kı-Hı relation

We first examine the Kı and Hı column density values reported by Hobbs (1974a, triangle markers in Figure 5). Hobbs (1974a) determined their opacity-corrected Hı column densities from Lyman$-\alpha$ absorption measurements obtained with the Orbiting Astronomical Observatory 2 (OAO-2, Savage & Jenkins 1972). Since Lyman$-\alpha$ absorption traces the total number of Hı atoms, it provides the "true" Hı column density along a line of sight, independent of spin temperature. Pearson and Spearman correlation analyses for their ten sightlines yield coefficients of 0.31 ($p-$value = 0.38) and 0.45 ($p-$value = 0.20), respectively. While both coefficients show positive trends, their associated $p-$values are well above the conventional significance threshold of 0.05. Due to their small sample size, we cannot confidently conclude the presence of a statistically significant linear or monotonic relationship between Kı and Hı based on Hobbs (1974a) data, as the observed trends could readily be attributed to random chance within such a limited dataset.

In contrast, our correlation analyses along 290 matched sightlines (within a 0.75 pc search radius) reveal a moderate positive relationship between opacity-corrected Hı and Kı column densities (indicated by circle markers in Figure 5). The Pearson correlation coefficient is $r = 0.36$, whereas the Spearman coefficient is $\rho = 0.43$. The correlation tests are highly statistically significant, with small $p-$values of $5 \times 10^{-10}$ and $4 \times 10^{-14}$, respectively. Using a larger sample of 403 sightlines (within a 1.5 pc search radius), we also find a moderate positive correlation between $N_{KI}$ and $N_{HI}$, though with slightly lower coefficients ($r = 0.34$, $\rho = 0.40$) and corresponding $p-$values
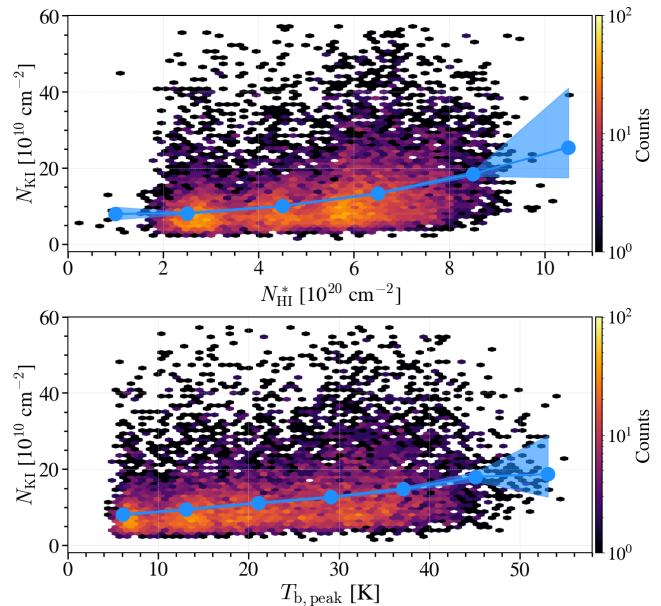


**Figure 6.** Correlations between Hı and Kı line-of-sight properties towards 9,821 stars in the Magellanic Cloud foreground. Top panel: Kı column density ($N_{KI}$) versus optically-thin Hı column density ($N_{HI}^*$). Bottom panel: Kı column density versus Hı peak brightness temperature ($T_{b,peak}$). Circles and shaded regions denote median values and their $1\sigma$ uncertainties per $N_{HI}^*$ and $T_{b,peak}$ bins, respectively. Color indicates data point density.

of $10^{-12}$ and $10^{-17}$. The statistical significance in both cases, supported by substantial sample sizes (290 and 403 sightlines), suggests a robust, though modest positive association between Hı and Kı. For comparison, Liszt (2021) found a Pearson correlation coefficient of 0.31 (see their Table 3) between $N_{KI}$ and $N_{HI}$ along five sightlines with both absorption detections, broadly consistent with our results.

We also search for the relations between $N_{KI}$ and other absorption-based tracers of cold Hı gas. We found a moderate positive correlation between $N_{KI}$ and the CNM optical depth ($\tau_{CNM}$ of the CNM components associated with the Kı absorption feature). The Pearson correlation coefficient is $r = 0.29$ with a highly significant $p-$value $= 8 \times 10^{-7}$, while the Spearman rank coefficient is $\rho = 0.22$ with $p-$value $= 1.5 \times 10^{-4}$. A similarly strong relationship is observed between $N_{KI}$ and the line-of-sight CNM column density ($N_{HI, CNM}$). Here, the Pearson coefficient is $r = 0.27$ with $p-$value $= 3 \times 10^{-6}$, and the Spearman coefficient is $\rho = 0.25$ with $p-$value $= 1.6 \times 10^{-5}$. The relationship between $N_{KI}$ and the Hı integrated optical depth ($\Upsilon_{HI}$) is slightly stronger with $r = 0.26$ ($p-$value $= 1.4 \times 10^{-5}$) and $\rho = 0.27$ ($p-$value $= 2.2 \times 10^{-7}$).

We then further examine the Hı-Kı line-of-sight properties for a larger sample of 9,821 selected sightlines (within the GASKAP-Hı observing footprint) using optically-thin Hı column density $N_{HI}^*$, peak brightness temperature $T_{b,peak}$ from Hı emission data, and Kı column density $N_{KI}$. An on-sky distribution of Kı column densities towards 9,821 stars, as shown in the left panel of Figure 1, reveals a distinctive spatial behavior. While the Kı column density distribution nicely follows the morphology of Hı filamentary structures characterized by high column densities ($N_{HI}^* > 5 \times 10^{20}$ cm$^{-2}$) and peak brightness temperature ($T_{b,peak} > 30$ K), it also scatters across the map. Figure 6 compares $N_{KI}$ with both $N_{HI}^*$ and $T_{b,peak}$; here, circle markers and shaded regions represent median values and $1\sigma$ uncertainties in column density and brightness temperature bins.
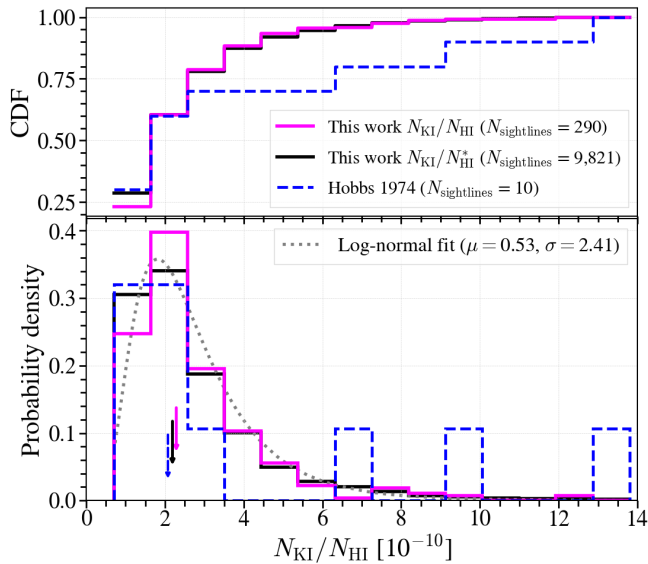
**Figure 7.** Distributions of KI/HI abundance ratios (lower panel), i.e. KI/HI column density ratios, and their cumulative distribution functions (CDF, upper panel). The solid magenta line represents our current work (290 lines of sight with optically-thick HI column densities), whereas the dashed line shows data from Hobbs 1974a (ten lines of sight). Arrows indicate the median values for each sample, at $\sim 2.3 \times 10^{-10}$ and $\sim 2.1 \times 10^{-10}$, respectively. The dotted curve represents the best-fit log-normal distribution ($\mu = 0.53$ and $\sigma = 2.41$) to the two combined KI/HI abundance ratios. For comparison, the solid black lines show the distributions for 9,821 lines of sight with optically-thin HI column densities, with its arrow indicating the corresponding median value $\sim 2.2 \times 10^{-10}$.

In these subsequent broader analyses, both Pearson and Spearman correlation tests indicate positive relationships between HI and KI properties. For the $N_{HI}^*$-$N_{KI}$ pair, the Pearson correlation coefficient is 0.30 ($p$−value $\ll 10^{-50}$), while the Spearman rank correlation is slightly higher at 0.37 ($p$−value $\ll 10^{-50}$). The correlation between $N_{KI}$ and $T_{b,peak}$ is similarly positive, with a Pearson coefficient of 0.28 ($p$−value $\ll 10^{50}$), and a Spearman coefficient of 0.33 ($p$−value $\ll 10^{50}$). The high statistical significance (indicated by extremely low $p$−values, effectively zero) across the latter analyses confirms that these positive HI-KI correlations are unlikely to be due to random chance. In all KI-HI column density comparisons carried out in this Section, the Spearman correlation coefficients are higher than their respective Pearson coefficients. This suggests that while $N_{KI}$ tends to increase as $N_{HI}$ (or $T_{b,peak}$) increases, their relationships might be better described by a general increasing trend rather than a linear one.

### 4.2 KI/HI abundance

The distribution of the resulting KI/HI abundance ratios across our sample of 290 matching lines of sight is presented in Figure 7, alongside a comparison to results derived from 9,821 sightlines using optically-thin HI column densities and to the findings of Hobbs 1974a (ten lines of sight). For the 290 matched sightlines, our analysis reveals a KI/HI abundance ratio ranging from $0.8 \times 10^{-10}$ to $12.7 \times 10^{-10}$, with a median (mean, standard deviation) of $2.3 \times 10^{-10}$ ($2.8 \times 10^{-10}$, $1.8 \times 10^{-10}$). Additionally, by leveraging the CNM properties derived from the GASKAP-HI absorption measurements (Nguyen et al. 2024), we estimate the ratio $N_{KI}/N_{HI, CNM}$

within our survey region, finding a median (mean and standard deviation) of $8.5 \times 10^{-10}$ ($13.8 \times 10^{-10}$ and $16.0 \times 10^{-10}$).

Across the 9,821 sightlines based on optically-thin assumption, the ratios $N_{KI}/N_{HI}^*$ range from $0.3 \times 10^{-10}$ to $41.1 \times 10^{-10}$, with a median (mean, standard deviation) of $2.2 \times 10^{-10}$ ($2.8 \times 10^{-10}$, $2.1 \times 10^{-10}$). For the ten lines of sight examined by Hobbs (1974a, see their Table 1), the reported KI/HI abundance ratios span from $0.7 \times 10^{-10}$ to $13.8 \times 10^{-10}$, with a median (mean, standard deviation) of $2.1 \times 10^{-10}$ ($4.2 \times 10^{-10}$, $4.2 \times 10^{-10}$). The excellent consistency between the statistical properties of the KI/HI abundance ratios derived from our significantly larger samples and those reported in literature provides strong support for the reliability of our KI abundance estimates and suggests a degree of uniformity in these ratios across different lines of sight probed by the two studies.

Given a small sample size of ten sightlines in Hobbs (1974a)'s sample, we perform a Mann–Whitney U test and two-sample Kolmogorov-Smirnov (KS) test to assess whether the Hobbs (1974a) sample and our 290-sightline sample originate from the same underlying distribution. The Mann–Whitney U test, which determines if there is a statistically significant difference between the medians of two independent groups, produces a U statistic of 1415, $p$−value = 0.9. The KS test produces a KS statistic of 0.3, $p$−value = 0.5. Both tests indicate there are no statistically significant differences between the two KI/HI abundance ratio distributions. We then fit three candidate probability distributions – exponential, log-normal, and gamma – to the combined KI/HI abundance ratios (with opacity-corrected $N_{HI}$). The log-normal distribution with $\mu = 0.53$ and $\sigma = 2.41$ provides the best fit (KS statistic = 0.06, $p$−value = 0.18), while the exponential and gamma distributions are strongly rejected, with KS statistic = 0.28 and 0.11, $p$−value = $2 \times 10^{-21}$ and $2 \times 10^{-3}$, respectively.

## 5 CONCLUSIONS AND FUTURE WORK

We have conducted a joint multi-wavelength analysis of the local neutral ISM with the use of two large-scale surveys: GASKAP for HI absorption at 21 cm and GALAH optical spectroscopy for KI absorption at 7699 Å. Leveraging the Gaussian decompositions performed by Nguyen et al. (2024) for 462 GASKAP lines of sight with HI absorption detections, together with GALAH measurements of interstellar KI absorption in the spectra of nearby stars by Buder et al. (2025), we investigated the kinematic relationship between CNM and neutral potassium in the Solar neighborhood at high Galactic latitudes ($-45°$, $-25°$) in the foreground of the Magellanic Clouds, as seen in Figure 1.

Our key findings are as follows:

(i) Along 462 GASKAP lines of sight with HI absorption detections, we identified 290 out of 462 ($\sim 63\%$) overlapping lines of sight showing absorption in both HI and KI neutral species.

(ii) We find a strong kinematic correlation between these two tracers of cold neutral ISM in the Magellanic Cloud foreground. The small velocity offsets ($\sim 1$ km s$^{-1}$) observed between corresponding HI and KI absorption features indicate a close physical association, suggesting that KI absorption likely arises within regions of cold hydrogen gas. In addition, a moderate positive correlation is found when examining HI and KI line-of-sight quantities, such as KI column density compared to HI column density, integrated optical depth, line-of-sight CNM column density or HI brightness.

(iii) Our derived KI/HI abundance ratio is in excellent agreement with previous measurements reported by Hobbs (1974a), with me-

dian ratios for the two samples, at ~2.3×10$^{-10}$ and ~2.1×10$^{-10}$, respectively

(iv) Our GASKAP-GALAH synergy highlights the power of combining large-scale radio and optical surveys to gain new insights into the structure and composition of the local neutral ISM.

Building upon strong H I-K I kinematic correlation found in this study, our future work will characterise the physical properties and spatial distribution of the local absorbing species across the sky, using H I absorption detected in all existing Galactic absorption surveys. A key next step will be to estimate distances to the detected H I gas features using the high-resolution GASKAP data in conjunction with detailed 3D dust maps of the Galactic ISM. Furthermore, we will establish a 3D field of H$\alpha$ emission by modelling the transport of H$\alpha$ photons and applying Gaussian inference to the well-constrained distances of nearby Solar neighborhood stars. By correlating the 3D distribution of H I and K I absorption with the derived 3D H$\alpha$ emission field, we will be able to investigate the ionization state of hydrogen gas and explore the interplay between neutral and ionized components of the local ISM on larger scales.

## DATA AVAILABILITY

This paper includes archived data obtained through the CSIRO ASKAP Science Data Archive, CASDA (https://research.csiro.au/casda).

All data related to the GALAH survey (https://www.galah-survey.org/) are publicly available at https://cloud.datacentral.org.au/teamdata/GALAH/public/GALAH_DR4/.

The GASKAP emission and absorption data used in this study, along with the fitted results and their associated uncertainties, are derived by Nguyen et al. (2024) and available at GASKAP Github repository.

All interstellar spectral data, their associated uncertainties, and the analysis notebooks used in this study are publicly available at (temporary) GitHub repository. A dedicated GASKAP Github repository and an official DOI will be provided upon publication acceptance.

## REFERENCES

Barden S. C., et al., 2010, SPIE, 7735, 09
Berkhuijsen E. M., Haslam C. G. T., Salter C. J., 1971, A&A, 14, 252
Brzeski J., Case S., Gers L., 2011, SPIE, 8125, 04
Buckland-Willis F., et al., 2025, A&A, 693, A239
Buder S., et al., 2025, PASA, 42, e051
Chen H., et al., 2025, AJ, 169, 284
Corliss C., Sugar J., 1979, Journal of Physical and Chemical Reference Data, 8, 1109
Cox D. P., Reynolds R. J., 1987, ARA&A, 25, 303
De Silva G. M., et al., 2015, MNRAS, 449, 2604
Dempsey J., McClure-Griffiths N. M., Jameson K., Buckland-Willis F., 2020, MNRAS, 496, 913
Dempsey J., et al., 2022, PASA, 39, e034
Di Teodoro E. M., et al., 2019, MNRAS, 483, 392
Dickey J. M., Kulkarni S. R., van Gorkom J. H., Heiles C. E., 1983, ApJS, 53, 591
Dickey J. M., et al., 2013, PASA, 30, e003
Dickey J. M., et al., 2022, ApJ, 926, 186
Draine B. T., 2011, Physics of the Interstellar and Intergalactic Medium
Edenhofer G., Zucker C., Frank P., Saydjari A. K., Speagle J. S., Finkbeiner D., Enßlin T. A., 2024, A&A, 685, A82
Erceg A., Jelić V., Haverkorn M., Bracco A., Ceraj L., Turić L., Soler J. D., 2024, A&A, 687, A23
Farrell T. J., Birchall M. N., Heald R. W., Shortridge K., Vuong M. V., Sheinis A. I., 2014, SPIE, 9152, 23
Field G. B., Goldsmith D. W., Habing H. J., 1969, ApJ, 155, L149
Gaia Collaboration et al., 2023, A&A, 674, A1
Gerrard I. A., et al., 2023, MNRAS, 526, 982

Górski K. M., Hivon E., Banday A. J., Wandelt B. D., Hansen F. K., Reinecke M., Bartelmann M., 2005, ApJ, 622, 759
HI4PI Collaboration et al., 2016, A&A, 594, A116
Heijmans J., et al., 2012, SPIE, 8446, 0W
Heiles C., Troland T. H., 2003, ApJS, 145, 329
Hobbs L. M., 1974a, ApJ, 188, L67
Hobbs L. M., 1974b, ApJ, 191, 381
Hunter J. D., 2007, Computing in Science & Engineering, 9, 90
Kalberla P. M. W., Haud U., 2018, A&A, 619, A58
Kennicutt R. C., Evans N. J., 2012, ARA&A, 50, 531
Kerp J., Winkel B., Ben Bekhti N., Flöer L., Kalberla P. M. W., 2011, Astronomische Nachrichten, 332, 637
Kos J., et al., 2017, MNRAS, 464, 1259
Lauroesch J. T., Meyer D. M., 1999, ApJ, 519, L181
Lee M.-Y., Stanimirović S., Murray C. E., Heiles C., Miller J., 2015, ApJ, 809, 56
Leike R. H., Glatzle M., Enßlin T. A., 2020, A&A, 639, A138
Lewis I. J., et al., 2002, MNRAS, 333, 279
Liszt H., 2021, arXiv e-prints, p. arXiv:2104.15013
Lynn C., et al., 2024, MNRAS
Ma Y. K., et al., 2023, MNRAS, 521, 60
Marchal A., Miville-Deschênes M.-A., Orieux F., Gac N., Soussen C., Lesot M.-J., d'Allonnes A. R., Salomé Q., 2019, A&A, 626, A101
McClure-Griffiths N. M., et al., 2009, ApJS, 181, 398
McClure-Griffiths N. M., et al., 2018, Nature Astronomy, 2, 901
McClure-Griffiths N. M., Stanimirović S., Rybarczyk D. R., 2023, Annual Review of Astronomy and Astrophysics, 61, null
McKee C. F., 1998, in Breitschwerdt D., Freyberg M. J., Truemper J., eds, , Vol. 506, IAU Colloq. 166: The Local Bubble and Beyond. pp 565–580
McKee C. F., Ostriker J. P., 1977, ApJ, 218, 148
McKinney W., et al., 2010, in Proceedings of the 9th Python in Science Conference. pp 51–56
Miszalski B., Shortridge K., Saunders W., Parker Q. A., Croom S. M., 2006, MNRAS, 371, 1537
Murray C. E., Stanimirović S., Goss W. M., Heiles C., Dickey J. M., Babler B., Kim C.-G., 2018, ApJS, 238, 14
Murray C. E., et al., 2024, ApJ, 962, 120
Nguyen H., Dawson J. R., Lee M.-Y., Murray C. E., Stanimirović S., Heiles C., Miville-Deschênes M. A., Petzler A., 2019, ApJ, 880, 141
Nguyen H., et al., 2024, MNRAS, 534, 3478
O'Neill T. J., Zucker C., Goodman A. A., Edenhofer G., 2024, arXiv e-prints, p. arXiv:2403.04961
Paszke A., et al., 2019, arXiv e-prints, p. arXiv:1912.01703
Pingel N. M., et al., 2022, PASA, 39, e005
Savage B. D., Jenkins E. B., 1972, ApJ, 172, 491
Schönrich R., Binney J., Dehnen W., 2010, MNRAS, 403, 1829
Sheinis A., et al., 2015, J. Astron. Telesc. Instrum. Syst., 1, 035002
Soler J. D., et al., 2019, A&A, 622, A166
Soler J. D., et al., 2025, A&A, 695, A222
Szotkowski S., et al., 2019, ApJ, 887, 111
Trapero J., Beckman J. E., Serra-Ricart M., Davies R. D., Watson R. A., Garcia Lopez R. J., 1995, ApJ, 445, 231
Trubko R., Gregoire M. D., Holmgren W. F., Cronin A. D., 2017, Phys. Rev. A, 95, 052507
Virtanen P., et al., 2020, Nature Methods, 17, 261
Vogrinčič R., et al., 2023, MNRAS, 521, 3727
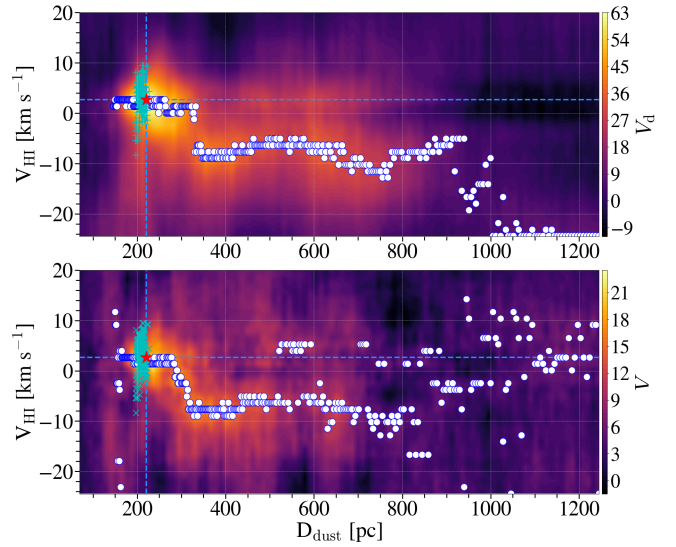Welty D. E., Hobbs L. M., 2001, ApJS, 133, 345
Winkel B., Kalberla P. M. W., Kerp J., Flöer L., 2010, ApJS, 188, 488
Wolfire M. G., McKee C. F., Hollenbach D., Tielens A. G. G. M., 2003, ApJ, 587, 278
Zhang X., Green G. M., Rix H.-W., 2023, MNRAS, 524, 1855
Zucker C., et al., 2022, Nature, 601, 334
van der Walt S., Colbert S. C., Varoquaux G., 2011, Computing in Science and Engineering, 13, 22

**Figure A1.** Morphological correlation between 3D dust distance channels and H I velocity channels for GASKAP's Galactic region $l = (270, 310)°$, $b = (-45, -25)°$. The correlation metrics are the direction-sensitive projected Rayleigh statistic ($V_d$ in upper panel) and the projected Rayleigh statistic ($V$ in lower panel). In both panels, circle markers indicate the velocity with the highest Rayleigh statistic values for each distance channel, star markers at the intersection of the dashed lines (at $D_{dust} = 220.3$ pc, $V_{HI} = 2.7$ km s$^{-1}$) indicates the velocity-distance pairs with the highest Rayleigh statistic across all velocity and distance ranges. Plus markers ("+") show velocity-distance matching from a simple matching between velocity at peak H I optical depth $\tau_{peak}$ and distance at peak dust extinction along 462 GASKAP lines of sight with H I absorption detections. Cross markers ("×") show velocity-distance matching from a simple matching between velocity at peak H I brightness temperature $T_{b,peak}$ and distance at peak dust extinction along the same H I absorption detection lines of sight.

## APPENDIX A: LINKING H I GAS TO PHYSICAL DISTANCE USING 3D DUST EXTINCTION AND HI4PI

In order to estimate physical distances to the local H I gas, we utilize the recently released 3D map of interstellar dust extinction by Edenhofer et al. (2024) in conjunction with the HI4PI data cube (HI4PI Collaboration et al. 2016).

The 3D dust map provides the distribution of differential extinction between 69 out to 1250 pc from the Sun. This map offers an angular resolution of ~13.7 arcmin (HEALPix[2] resolution parameter $N_{side}$ = 256) and a distance resolution of 2 pc. Built upon Gaia mission data (Gaia Collaboration et al. 2023), the 3D dust reconstruction employs a Gaussian process to model differential dust extinction in spherical coordinates for 54 million nearby stars, assuming a spatially smooth distribution of dust extinction. The differential extinction is given in unitless values, defined by Zhang et al. (2023) (hereafter ZGR23) as ($dA_{ZGR23}/1$ pc). These extinction units can be converted into extinction at a specific wavelength using the publicly available ZGR23 extinction curve[3].

For H I emission, we employ the HI4PI data cube, constructed from the Effelsberg-Bonn H I Survey (EBHIS; Winkel et al. 2010; Kerp et al. 2011) and the Galactic All-Sky Survey (GASS; McClure-Griffiths et al. 2009) single-dish observations. The combined set has

[2] The Hierarchical Equal Area isoLatitude Pixelization (Górski et al. 2005).
[3] ZGR23 extinction curve: DOI 10.5281/zenodo.7811871
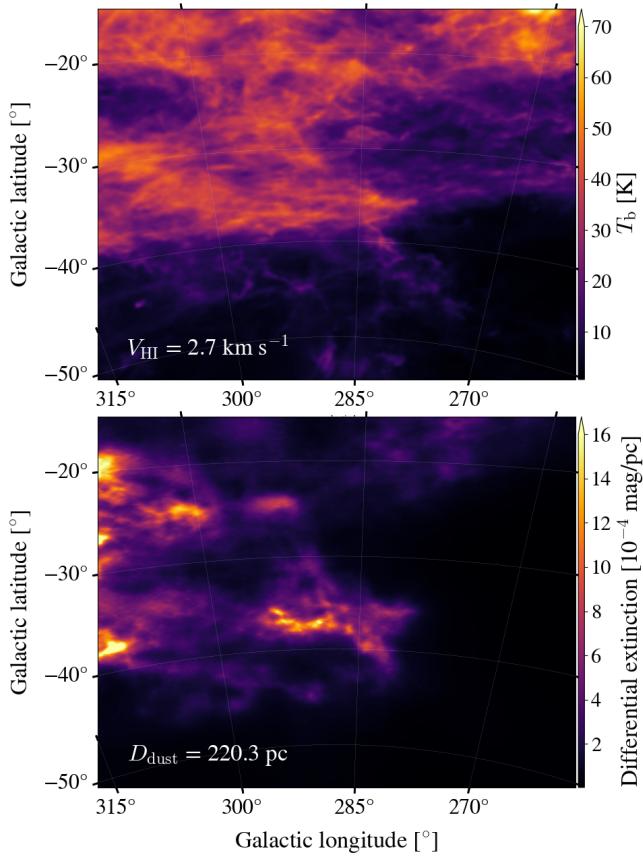
**Figure A2.** [Placeholder here, the axes are not correct! Juan is updating this!] H I velocity and dust distance channels with highest morphological correlation. This example corresponds to the highest $V_d$ (and $V$) in the comparison between the H I emission and the 3D dust extinction presented in Figure A1. *Left*: HI4PI emission at velocity $V_{HI} \approx 2.7$ km s$^{-1}$. *Right*: Dust differential extinction at distance $D_{dust} \approx 220.3$ pc obtained from Edenhofer et al. (2024).

an angular resolution of 16.2 arcmin and a sensitivity of 43 mK per 1.29 km s$^{-1}$ spectral resolution. This angular resolution is close to the 14 arcmin resolution of the 3D dust map. Assuming H I kinematics as a proxy for the gas physical distances, these comparable resolutions potentially allow for an informative morphological comparison between dust extinction and H I emission structures.

We then apply the Histogram of Oriented Gradients (HOG) method (Soler et al. 2019) to the gas and dust cubes to identify spatial correlations between the two ISM tracers. This method is originally designed to characterise the similarities in the emission distribution based on gradient orientations. In this work, HOG analysis quantifies the morphological similarity between the 2D plane-of-the-sky distribution of the 3D dust extinction and H I emission. This is done by comparing distance channels ($D_{dust}$ in pc) from dust map with velocity channels ($V_{HI}$ in km s$^{-1}$) from H I data. A velocity channel map and a distance channel map are considered morphologically similar if their gradients are mainly parallel, and dissimilar if they exhibit randomly oriented. Specifically, for each pair of H I velocity and dust distance maps, the HOG method produces the projected Rayleigh statistic ($V$, see Soler et al. 2019) and the direction-sensitive projected Rayleigh statistic ($V_d$, see Soler et al. 2025) to quantify the relationship between the 3D dust and H I emission.

The Rayleigh statistic ($V$ or $V_d$) assesses non-uniformity in a distribution of angles around a specific direction. A positive Rayleigh

statistic indicates that the gradients are primarily parallel, signifying a morphological similarity between the H I emission and dust extinction in the corresponding velocity-distance channel pair. In contrast, a negative Rayleigh statistic suggests that the gradients are mostly antiparallel, leading to an anti-correlation between the dust extinction and H I emission intensity.

In this Section, we consider the local gas in the high galactic-latitude Cirrus region $l = (270, 310)°$, $b = (-45, -25)°$ with velocity range from $-25$ to $+25$ km s$^{-1}$, and the dust distance from 69 to 1250 pc from the Sun. Figure A1 illustrates the HOG morphological correlation between velocities from H I emission observations and distances from 3D dust extinction reconstruction for our region of interest. The upper panel displays the velocity-distance correlations with the direction-sensitive projected Rayleigh statistic $V_d$ colour-coded, the lower panel for the same correlations but for the projected Rayleigh statistic $V$. Following Soler et al. (2025), $V_d$ values at $\sim 0$ indicates a random orientation and low morphological correlation between the gradients of the two tracers. Values of $V_d > 2.87$ suggest mostly parallel gradients and a significant morphological correlation, whereas $0 < V_d < 2.87$ indicate mostly antiparallel gradients. Within each distance channel, white dots mark the velocity with the highest Rayleigh statistic values. Star markers denote the velocity-distance pairs with the highest Rayleigh statistic across all velocity and distance ranges. In both panels they are exactly at the same velocity-distance pairs $D_{dust} = 220.3$ pc, and $V_{HI} = 2.7$ km s$^{-1}$, although the white dots are more dispersed for the $V$ Rayleigh statistic values, in particular at closer distances $D_{dust} < 170$ pc. Figure A2 presents an example of H I emission along with dust extinction distribution, for the velocity-distance pair that obtains the highest morphological correlation as identified by the peak $V_d$ and $V$ values in Figure A1.

In addition to the HOG approach, we performed a simple velocity-distance matching. This involved comparing the velocity at peak H I optical depth ($\tau_{peak}$) with the distance at peak dust extinction along 462 GASKAP lines of sight with H I absorption detections. We also matched the velocity at peak H I brightness temperature ($T_{b,peak}$) with the distance at peak dust extinction along the same lines of sight. These simple matchings are represented by plus ("+") and cross ("×") markers in the upper and lower panels of Figure A1, respectively. Both HOG analysis and simple velocity-distance matching indicate that the distances to local H I gas in the direction of the Magellanic Cloud foreground range from 160 pc to 260 pc, with a likely distance $\sim 220$ pc and a corresponding H I gas velocity of $\sim 3$ km s$^{-1}$.

This paper has been typeset from a TEX/LATEX file prepared by the author.